A 1.0-THz High-Gain Metal-Only Transmit-Array Antenna Based on High-Precision UV-LIGA Microfabrication Technology

Zhuo-Wei Miao, *Member, IEEE*, Zhenhao Liu, Zhang-Cheng Hao, *Senior Member, IEEE*, Yongbin Zeng, Di Zhu, Jia-Hui Zhao, *Student Member, IEEE*, Chen-Yu Ding, *Student Member, IEEE*, Li Cheng, Lei Zhao, *Senior Member, IEEE*, and Wei Hong, *Fellow, IEEE*

***Abstract*—Implementing high-gain antennas operating in exceedingly high THz regions, e.g., the challenging WR-1.0 band, relies significantly on dependable microfabrication technologies. Due to the advantages of high precision, low cost, and high uniformity, this article presents a 1.0-THz 64 × 64-element high-gain metal-only transmit-array (TA) antenna fabricated using ultraviolet photolithography techniques in conjunction with micro electroforming (collectively, UV-LIGA). As a highly parallel batch fabrication technology, the UV-LIGA consists of three main stages in this case, namely film fabrication, electroforming, and assembly. In full consideration of array structural stability and intrinsic connectivity based on the UV-LIGA, the proposed phasing element design employs a five-layered folded-slot structure with four air-filled spacer layers. By placing a shim layer between two contiguous folded-slot slices, whose thickness can be varied by modifying the electroforming time, each air gap can be accurately and flexibly ensured. The fabricated TA prototype is experimentally validated in a THz chamber. The maximum gain is 36.47 dBi, and its corresponding aperture efficiency is equal to 25.96%. The measured 3-dB gain bandwidth is from 0.79 to 1.03 THz.**

***Index Terms*—1.0 THz, high gain, metal-only, microfabrication technology, transmit-array (TA) antenna, UV-LIGA.**

Manuscript received 17 September 2023; revised 31 October 2023; accepted 18 November 2023. Date of publication 1 December 2023; date of current version 5 March 2024. This work was supported in part by the National Natural Science Foundation of China under Grant 62101119, Grant 62131008, and Grant 62331018, in part by the National Key Research and Development Program of China under Grant 2019YFB1803202, in part by the China Postdoctoral Science Foundation fund project under Grant 2022M710025, in part by the Youth Talent Promotion Foundation of Jiangsu Science and Technology Association TJ-2022-095, in part by the Natural Science Foundation of Jiangsu Province under Grant BK20222010, and in part by the Fundamental Research Funds for the Central Universities under Grant 2242022k30003. *(Corresponding authors: Zhang-Cheng Hao; Yongbin Zeng.)*

Zhuo-Wei Miao, Jia-Hui Zhao, and Chen-Yu Ding are with the State Key Laboratory of Millimeter-Waves, the Frontiers Science Center for Mobile Information Communication and Security, School of Information Science and Engineering, Southeast University, Nanjing 210096, China (e-mail: zwmiao@seu.edu.cn; jhzhao@seu.edu.cn; cyding_aly@seu.edu.cn).

Zhenhao Liu, Yongbin Zeng, and Di Zhu are with the National Key Laboratory of Science and Technology on Helicopter Transmission, Nanjing University of Aeronautics and Astronautics, Nanjing 210016, China (e-mail: lzh2000ing@163.com; binyz@nuaa.edu.cn; dzhu@nuaa.edu.cn).

Zhang-Cheng Hao and Wei Hong are with the State Key Laboratory of Millimeter-Waves, the Frontiers Science Center for Mobile Information Communication and Security, School of Information Science and Engineering, Southeast University, Nanjing 210096, China, and also with Purple Mountain Laboratories, Nanjing 211100, China (e-mail: zchao@seu.edu.cn; weihong@seu.edu.cn).

Li Cheng is with the Nanjing Research Institute of Electronic Technology, Nanjing 210039, China (e-mail: chengli1@cetc.com.cn).

Lei Zhao is with the School of Information and Control Engineering, China University of Mining and Technology, Xu Zhou 221116, China (e-mail: leizhao@cumt.edu.cn).

Color versions of one or more figures in this article are available at https://doi.org/10.1109/TTHZ.2023.3338473.

Digital Object Identifier 10.1109/TTHZ.2023.3338473

I. Introduction

THE utilization of terahertz (THz) spectrum (0.1–10 THz) has shown to be a promising solution to satisfy the imperative need for high data transmission rates and a huge capacities in next-generation ultrahigh-speed wireless communications [1], [2], [3]. To compensate for severe propagation attenuation by the atmosphere and low output power of THz sources, THz wireless transceiver front-ends always involve antennas with high-gain performance; otherwise, the communication quality of the entire THz system would be substantially compromised [4], [5]. Driven by this pressing necessity, numerous efforts have been made to develop THz high-gain antennas recently, including horn antennas [6], [7], [8], [9], planar antenna arrays [10], [11], [12], [13], [14], [15], reflection-type antennas [16], [17], [18], [19], [20], [21], [22], and transmission-type antennas [23], [24], [25], [26], [27], [28], [29], [30], [31], [32].

In order to efficiently radiate THz waves with high gain (e.g., over 35 dBi), horn antennas typically involve bulky sizes and are challenging to integrate with THz transceiver front-ends, whereas planar antenna arrays constantly suffer from complicated feeding networks with a considerable loss [33]. Without these disadvantages, curved dielectric lens antennas have been widely used for gain enhancement in many practical THz systems [34], [35]. Flat transmit-arrays (TAs) have recently come to the forefront as a new iteration of lens antennas, well-developed at the frequency bands below 0.1 THz [36], [37], [38], [39]. Several conventional manufacturing technologies, such as three-dimensional (3-D) printed technology [27], [28], printed circuit board (PCB) technology [29], [30] and low temperature cofired ceramics (LTCC) technology [31], [32], can still allow for the fabrication of TA antennas working at low THz regions, typically lower than 0.3 THz. As the operating frequency rises to high THz bands, e.g., the challenging WR-1.0 band (0.75–1.1 THz), geometrical accuracy and machining tolerance during the manufacture become formidable obstacles [40].

2156-342X © 2023 IEEE. Personal use is permitted, but republication/redistribution requires IEEE permission.
See https://www.ieee.org/publications/rights/index.html for more information.

Authorized licensed use limited to: CHINA UNIVERSITY OF MINING AND TECHNOLOGY. Downloaded on March 07,2024 at 00:09:57 UTC from IEEE Xplore. Restrictions apply.

Therefore, implementing high-quality WR-1.0 TAs requires dependable parallel-micromachining techniques.

Lithography-based micromachining techniques can produce geometric features on a size of a few microns, which have been widely used in the implementation of TAs above the WR-1.0 band [41], [42]. In order to achieve high transmission efficiency and enough phase-shift coverage, these THz TAs usually consist of multilayer metallic structures separated by dielectric substrates [43]. However, some substrates, such as polyimide layers employed in [41] and [42], exhibit a high dielectric loss tangent of 0.05 at THz regions, which decreases the radiation efficiency of the THz TA devices. In comparison, metal-only construction would not only result in zero dielectric loss, but it would also demonstrate high-thermal conductivity and stable performance in harsh environments. Recent research interest in antenna engineering has been focused on metal-only TAs, an essential member of the TA family [44], [45], [46], [47], [48], [49]. Notably, a multilayered metal-only TA antenna has been successfully extended beyond 0.3 THz [49]. However, limited progress has been made in high-gain metal-only TAs operating at or above the 0.75–1.1 THz band as a result of the significant challenges in their microfabrication. Conventional micromachining techniques, such as lithography and reactive ion etching, can only be used to process films with a thickness of a few micrometers [22], [49]. With such a thin metallic layer, high-gain metal-only TAs with electrically large radiation apertures have a tendency to deform and stress delicate features, making their practical application difficult due to poor structural stability. Consequently, a large demand has emerged for THz metal-only TAs with a thickness of dozens of microns for each metal layer, necessitating the exploration of manufacturing techniques to construct high aspect-ratio microstructures (HARMs) with high precision and low surface roughness.

Lithographie, Galvanoformung, and Abformung (LIGA) is widely recognized as a highly advanced and adaptable microfabrication process. By exposing thick photoresists to particular light sources, 3-D molds for the electroforming of metallic HARMs can be built with arbitrary 2-D patterns [50]. Particularly if a conventional and economical ultraviolet source is used to expose epoxy-based SU-8, the so-called UV-LIGA is a prospective solution for implementing THz metallic HARMs owing to its high resolution and high manufacturing quality [51]. To validate the UV-LIGA's suitability for THz applications, this article presents a high-gain, metal-only, multilayered TA antenna near 1.0-THz frequencies. It should be noted that a high aspect-ratio close to 20:1 can be achieved by the UV-LIGA, well-suited for fabricating THz TAs with a thickness of tens or hundreds of microns for each metal layer. In addition to structural thickness, intrinsic connectivity must be prioritized when designing metal-only arrays. According to these characteristics, a five-layered folded-slot structure with four air-filled spacer layers is chosen as the TA phasing element. The manufacturing process for all these metallic layers contains three fundamental subprocesses: film fabrication, micro copper electroforming, and precise assembly. To our knowledge, UV-LIGA-based metal-only TA antennas in the 1.0-THz band have not yet been reported. The proposed antenna is the first exploration of the UV-LIGA technique for the realization of metal-only TAs operating in the WR-1.0 band. The effective implementation and measurement of the proposed metal-only TA antenna demonstrate the viability and superiority of the UV-LIGA technique in this high THz region.

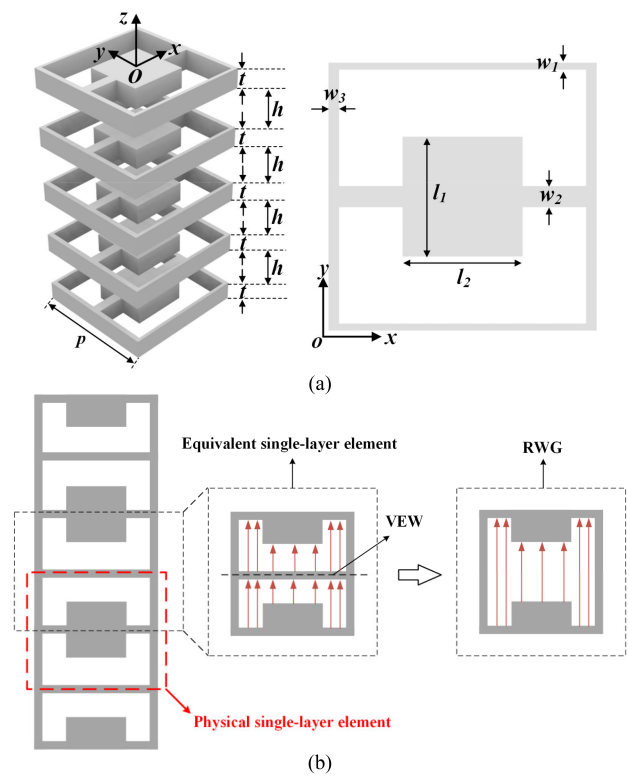

Fig. 1. (a) Geometry of the metal-only TA element and its parameters. (b) Equivalent model of the unit cell based on the theory of RWGs.

II. Design of the Metal-Only Unit Cell and the TA

A. Design of the THz Metal-Only Unit Cell

When designing a THz high-gain metal-only TA antenna in the challenging 0.75–1.1 THz band, physical realizability and structural stability should take precedence. On the basis of careful consideration of the UV-LIGA's characteristics, a simple multilayer-frequency-selective-surface (MFSS) element structure is proposed for the TA. As shown in Fig. 1(a), the proposed phasing element is comprised of two parts: identical all-metal layers and air spaces between contiguous metallic layers. Copper is chosen for the conductor layers in this design due to its high electrical conductivity. The overall design of each metallic layer is based on two main rectangular slots, each with one notch near the center of the TA phasing element. The two folded segments, controlled by these parameters l_1, l_2, w_1, w_2, and w_3, are symmetric regarding the x-axis. It has been revealed in [43] that an MFSS TA element must involve at least four identical metallic layers in order to achieve a transmission phase coverage over 360° with a −1-dB transmission magnitude. In addition to the transmission performance, the intrinsic connectivity and mechanical strength of the copper layer must be considered as well because of the absence of a substrate

Authorized licensed use limited to: CHINA UNIVERSITY OF MINING AND TECHNOLOGY. Downloaded on March 07,2024 at 00:09:57 UTC from IEEE Xplore. Restrictions apply.

TABLE I
GEOMETRIC PARAMETERS OF THE PROPOSED THZ TA UNIT CELL

Parameter	Value (μm)	Parameter	Value (μm)
p	190	h	60
t	30	w_1	5
l_1	15–107	w_2	15
l_2	85	w_3	7.5

to sustain the structure; therefore, each layer's thickness is set to 30 μm, approximately one-tenth of its wavelength near 1.0 THz. However, the transmission performance of the MFSS TA element is diminished due to the relatively large thickness of each layer. To obtain adequate phase coverage over 360° with an acceptable transmission magnitude, it is necessary to employ a five-layer topology in the proposed MFSS TA element design.

Due to the thickness of each metallic layer comparable to the wavelength near 1.0 THz, it is not feasible to employ a simple capacitance-inductance circuit as an equivalent model for the TA element. The waveguide mode must be taken into consideration. In fact, the design of the proposed TA element is inspired by ridge waveguides (RWGs). As shown in Fig. 1(b), the single-layer array can be conceptualized as a periodic arrangement of "equivalent elements." According to the electric field distribution and the mirror principle, the metallic partition in each equivalent element can be regarded as a virtual electric wall (VEW), and its presence or absence has no effect on the electric field distribution. In other words, the metal partition can greatly improve the structural stability of the TA in addition to having no effect on the field distribution. Therefore, the equivalent elements can be considered a RWG, and its phase modulation capability can be explained using RWG theory. The RWG can be viewed as rectangular waveguides with the elongated side bent. Similar to modifying the dimensions of the longer side of a rectangular waveguide, changing the height of the ridge is analogous to modifying the length of the ridge. The phase velocity of THz waves propagating within the waveguide undergoes variations as the longer side assumes different diameters, leading to discernible phase shifts along the same route. In summary, the proposed element shares similarities with the adjustment of ridge height, thereby facilitating a wide range of phase modulation capabilities through the sequential integration of five identical layers.

The proposed metal-only MFSS TA element is numerically analyzed utilizing the Method of Moments solver with periodic boundary conditions in the commercial full-wave software FEKO. The final geometric parameters after full-wave optimization are presented in Table I. The periodicity of the TA unit cell is finalized as 190 μm. The proposed metal-only unit cell responds exclusively to the y-polarized incident waves, as shown in Fig. 2; consequently, a high transmissivity with high polarization purity can be attained. Its cross-polarization level (CPL) exceeds over 80 dB throughout the entire operational THz spectrum. By varying the notch length of each slot controlled by the parameter l_1, transmission phase responses can be fully controlled when the phasing element is illuminated by a y-polarized electromagnetic wave. The simulated responses

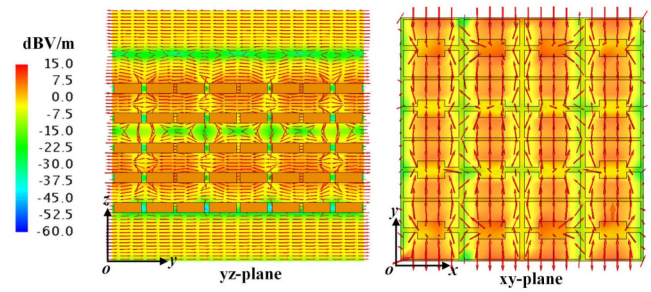

Fig. 2. Distributions of the induced electric field for a 16-element subarray with periodic boundary conditions at 0.9 THz when the parameter l_1 is set to 55 μm.

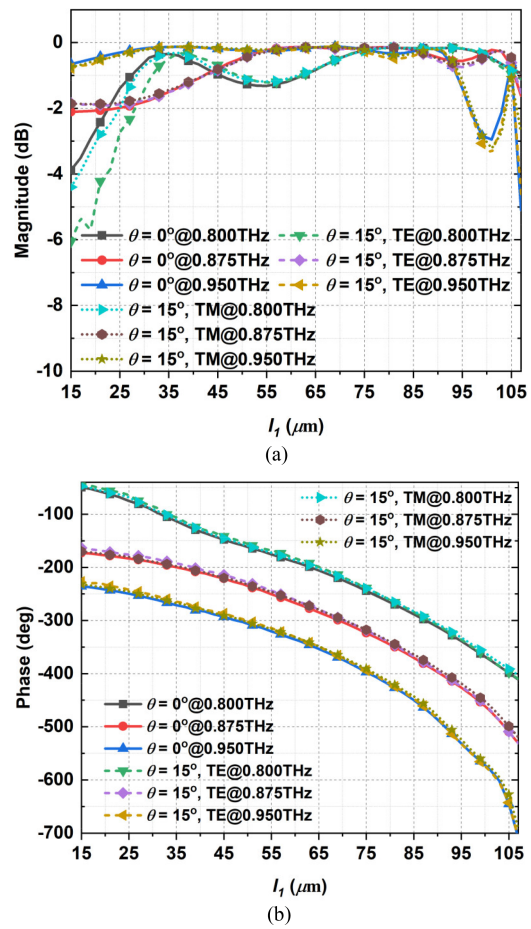

Fig. 3. Simulated results of the metal-only TA unit cell under normal and 15° oblique y-polarized illuminations at different THz frequencies when the parameter l_1 is swept from 15 to 107 μm. (a) Transmission magnitude. (b) Transmission phase.

of the five-layer metal-only unit cell under normal and 15° oblique y-polarized excitations are depicted in Fig. 3 for various notch lengths. Table II provides a summary of the simulated phase and magnitude results. By changing the parameter l_1 from 15 to 107 μm, a 360° phase variation coverage can be achieved across the frequency spectrum from 0.8 to 0.95 THz. Given that the focal length to diameter ratio (F/D) of this design is 2.25, the maximum angle of feed illumination cannot exceed 15°. Fig. 3(b) also provides the simulated results of phase responses

Authorized licensed use limited to: CHINA UNIVERSITY OF MINING AND TECHNOLOGY. Downloaded on March 07,2024 at 00:09:57 UTC from IEEE Xplore. Restrictions apply.

TABLE II
BRIEF SUMMARY OF THE SIMULATED RESPONSE OF THE TA ELEMENT

Frequency (THz)	0.800		0.875		0.950	
Response	Mag (dB)	Phase (°)	Mag (dB)	Phase (°)	Mag (dB)	Phase (°)
Normal incidence	-0.84	>360	-0.76	>360	-0.54	>360
Oblique incidence (TE)	-1.06	>360	-0.76	>360	-0.59	>360
Oblique incidence (TM)	-0.86	>360	-0.73	>360	-0.53	>360

Note: The simulated magnitude results in Table II are averaged when the parameter l_l changes from 15 to 107 μm by the step of 2 μm.

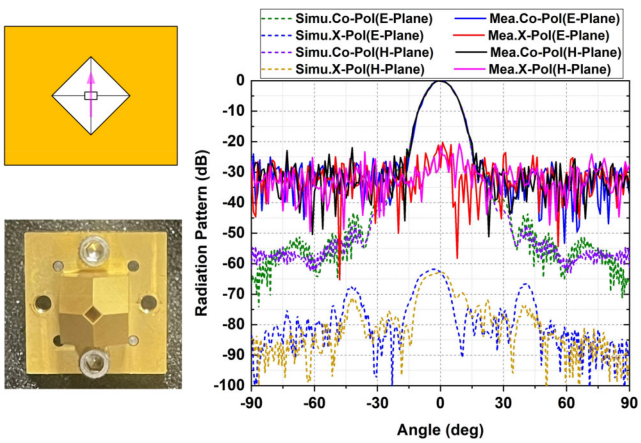

Fig. 4. Photography of the diagonal horn antenna with its normalized radiation patterns at 0.9 THz [52].

when a TE or TM source with an oblique incidence excites the TA element. For the cases of $(\theta, \varphi) = (15°, 0°)$ and $(\theta, \varphi) = (15°, 90°)$, the proposed metal-only TA element exhibits a stable performance with acceptable phase variation. It can be shown that the phase response curves under a normal illumination and a 15° oblique incidence deviate by no more than 10°. Thus, the proposed metal-only unit cell is suitable for the THz TA design working at the WR-1.0 band.

B. THz Feed Source and the Design of the TA

The feed source is another critical component of a TA antenna system. Due to their superior radiation performance, metallic horn antennas have been extensively employed in practice. In this THz TA design, a commercial diagonal horn antenna, manufactured by Virginia Diodes Inc. (VDI), is employed as the feed source [52]. The dimensions of the feed port for the diagonal horn are 254 μm × 127 μm. Its aperture diameter and length are 1.6 mm and 16 mm, respectively. Fig. 4 provides the radiation patterns of the diagonal horn antenna. The simulation and measurement of the radiation patterns' main beams show good agreement with an equal flare angle of roughly 15°. Half-power beam widths (HPBWs) in the E-plane and H-plane are measured to be 11.4° and 11.6°, respectively. In terms of CPLs and areas outside of the primary beams, however, there are discernible differences between the simulation and measurements. This is due to a combination of factors, including the THz VDI vector network analyzer's low dynamic range and the diagonal horn antenna's insufficient power level for polarization separation.

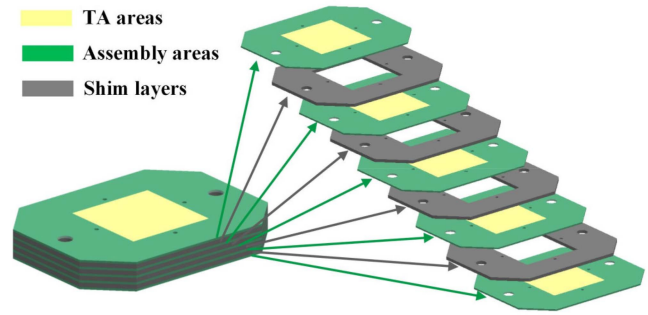

Fig. 5. Diagram of the proposed THz metal-only TA.

A five-layer metal-only THz TA with a square radiation aperture of 12.16 mm × 12.16 mm is designed using the proposed unit cell. This aperture is excited by the diagonal horn, whose phase center should coincide with the focal point. Considering the relatively narrow HPBWs of the diagonal feed horn, the F/D ratio is set to 2.255 to provide proper illumination [31], resulting in a maximal incident wave oblique angle of approximately 12.5°. According to [45], the desired phase compensation value for each phasing element can be determined by

$$\varphi_{pq} = k \times (r_{fpq} - F) + \varphi_0 \tag{1}$$

where the parameter r_{fpq} denotes the distance between the unit cell marked with pqth and the feed source, the constant k is the free space wavenumber, and the parameter φ_0 represents the phase of the central element. Therefore, the structure of the metal-only TA can be determined.

III. FABRICATION OF THE METAL-ONLY TA

As shown in Fig. 5, the proposed metal-only TA is composed of five stacked metallic layers with folded slot and four air-filled spacer layers. In this work, TA molds based on SU-8 photoresist can be generated using UV-LIGA technology; after electroforming, the thickness of each slot layer and each spacer layer is 30 μm and 60 μm, respectively. Using a low-cost UV source, this micromachining technique enables the fabrication of features as small as a few microns or even smaller. Fig. 6 illustrates the micromachining process of the UV-LIGA technique for creating the THz metallic TA layer with folded-slot structure, including the film fabrication, the copper electroforming, and assembly. The fabrication of the shim layer can use the same process.

A. Film Fabrication

Due to its superior mechanical, physical, and chemical corrosion resistance capacity and optical properties, SU-8, an epoxy-based negative photoresist, is widely used in the UV-LIGA micromachining procedure. A minor quantity of photo-acid generator is present in the SU-8 photoresist, then the SU-8 produces a potent acid after photon absorption. This photoacid is capable of catalyzing the subsequent cross-linking reaction

Authorized licensed use limited to: CHINA UNIVERSITY OF MINING AND TECHNOLOGY. Downloaded on March 07,2024 at 00:09:57 UTC from IEEE Xplore. Restrictions apply.

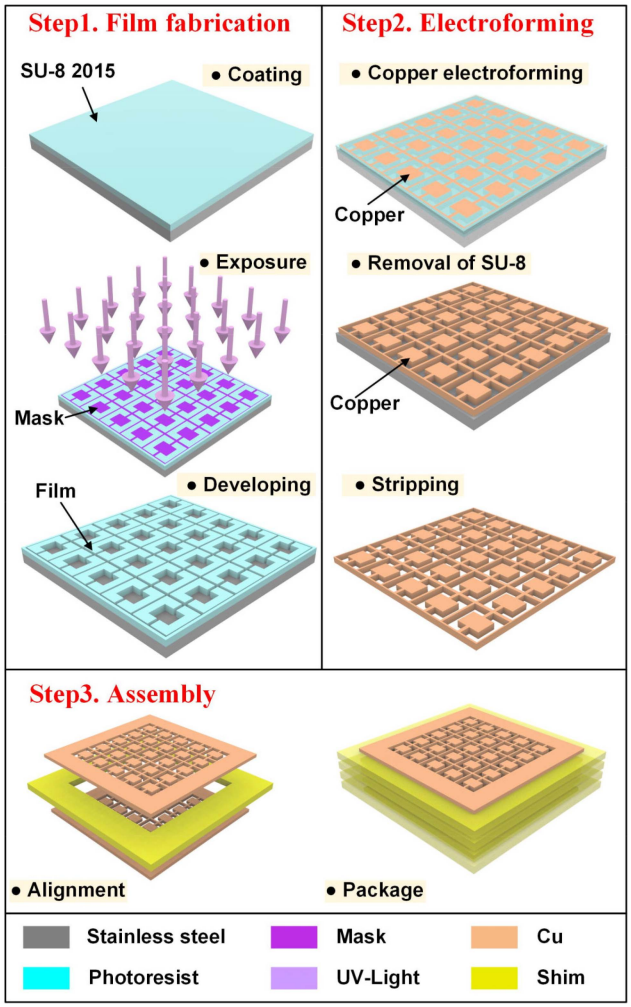

Fig. 6. UV-LIGA process for generating the THz metal-only TA device.

TABLE III
OPTIMIZED PROCESS PARAMETERS FOR THE FILM FABRICATION

Subprocess	Name	Method and time	Material or instruments
1	Coat	800 r/min for 10 s;	SU-8 2015
2	Soft bake	65 °C for 90 s; 95 °C for 15	Level hotplate
3	Expose	20 mW·cm^{-2} for 7 s	SUSS MJB4
4	PEB	65 °C for 90 s; 95 °C for 9 min;	Level hotplate
5	Develop	24 °C for 5 min	MicroChem's developer; IPA

that occurs during the post-exposure bake (PEB). In this article, the photoresist SU-8 2015 is employed for the fabrication of the proposed TA structure. SU-8 2015 is capable of manufacturing structures with a thickness of dozens of microns and has outstanding imaging properties. The detailed subprocesses for the film fabrication are summarized in Table III.

The TA film fabrication begins with the preparation of a 5-inch 304 Mirror Stainless-Steel wafer, which requires no conductivity treatment and has a surface with exceptionally low roughness. Before evenly coating the SU-8 photoresist, the wafer must be pretreated. A clean and arid wafer surface is conducive to the complete hydration of the photoresist and substrate, enhancing the bonding force between the two and preventing the occurrence of undercutting. Once the photoresist is chosen, the coating thickness H is dependent on the spin speed ω, which can be expressed as

$$H \propto \frac{1}{\sqrt{\omega}}. \tag{2}$$

The coating with SU-8 2015 photoresist includes two stages to assure the desired thickness, 800 r/min for 10 s and 1100 r/min for 30 s, respectively, as determined by our repeated experiments.

After coating, the resist layer must be soft-baked to remove the solvent. The duration of the soft bake is dependent on the solvent concentration of the photoresist. For the lesser duration of the soft bake subprocess, the layer can be softer with insufficient correction of spinning coating defects. However, if there is an excessive amount of residual solvent, photoacid molecules may diffuse beyond the borders of the pattern, resulting in a decrease in geometry resolution. In contrast, an extended soft bake period leads to the photoresist layer to harden, facilitating separation from the wafer and increasing the likelihood of the layer splitting. Consequently, the condition of soft bake must be handled carefully, taking into account its effect on the SU-8 solvent evaporation, process parameter optimization, and the accuracy of geometry resolution. In this article, the UV-LIGA entails a soft bake consisting of two stages at 65 °C for 1.5 min and 95 °C for 15 min on a level hotplate, respectively.

Based on the structure of the proposed TA, a specific photolithography mask is customized for UV exposure. The exposure dose E is determined by the product of the exposure intensity I_0 and the corresponding exposure time. It should be noted that the difference between the ideal exposure and structures with excessive cross-linking owing to the displacement of the focal plane can be as small as $\pm$ 5%. On the one hand, the SU-8 thickens as a result of overtime exposure, which is ascribed to UV scattering and diffraction, and the sidewalls are uneven owing to a greater dose of exposure on the upper side compared to the lower side; on the other hand, the effect of bottom undercut cannot be avoided if the exposure duration is insufficient. Thus, many efforts must be made to carefully determine the exposure intensity and exposure time. In this work, the alignment and exposure are performed using the MJB4 mask aligner. After some experiments, the patterns were produced using a dosage of 140 mJ·cm^{-2}, and the corresponding time is 7 s.

During the PEB, the photoacid produced by UV exposure undergoes a cross-linking reaction, thereby solidifying the exposed region on the wafer. The PEB can result in fracture or delamination of the SU-8 structures if the temperature is ramped too rapidly, as the stresses have not had sufficient time to be alleviated. Hence, a two-stage PEB on a level hotplate was used. The wafer was first heated from room temperature to 65 °C at 3 °C/min, held at 65 °C for 1.5 min; then, the temperature was increased to 95 °C and held for 9 min. It is worth noting that the duration of the PEB must be accurately controlled. The

Authorized licensed use limited to: CHINA UNIVERSITY OF MINING AND TECHNOLOGY. Downloaded on March 07,2024 at 00:09:57 UTC from IEEE Xplore. Restrictions apply.

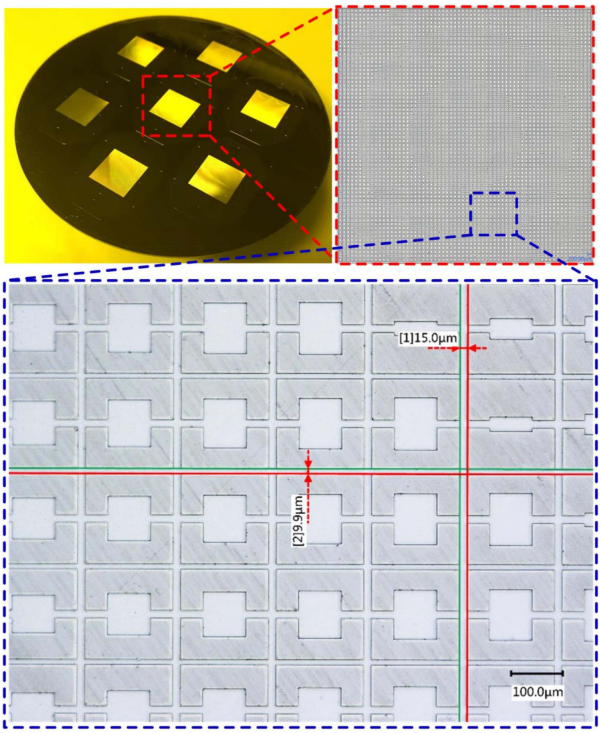

Fig. 7. Photography of the fabricated TA film.

TABLE IV
INGREDIENTS OF THE COPPER ELECTROFORMING ELECTROLYTE

Bath constituent	Functions	Concentration
$CuSO_4 \cdot 5H_2O$	Supply Cu^+	200 g/L
H_2SO_4	Enhance the solution's conductivity and dispersion ability; Dissolve the anode	70 g/L
Chloride ion	Enhance the layer's uniformity; Minimize internal tension	50 mg/L

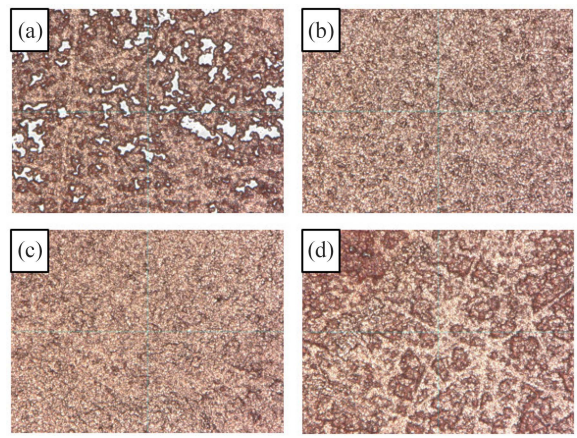

Fig. 8. Photomicrograph of the electroformed copper surfaces under different dc current densities. (a) 0.5 A/dm^2. (b) 1.5 A/dm^2. (c) 2.5 A/dm^2. (d) 3.5 A/dm^2.

T-shaped structure in the SU-8 layer will fracture and be difficult to remove if the photoresist is overbaked; by contrast, if the PEB is insufficient, the SU-8 molecules will not cross-link adequately.

A commercially available SU-8 developer, also known as PGMEA, selectively dissolves the uncross-linked photoresist from the wafer. The UV-exposed SU-8 can be maintained intact. During the experiment, the samples were immersed in a bath with PGMEA. It should be pointed out that the SU-8 will swell during the development. As long as concave rubber pieces adjacent to one another expand by 6%, narrow fissures will adhere completely. In this case, the samples can be completely developed at the temperature of 24 °C for 5 min. The isopropyl alcohol (IPA) can be used to analyze the development process. An incompletely developed adhesive film immersed in IPA may contain white impurities.

Fig. 7 presents the pattern after the development. The 5-inch wafer is capable of accommodating seven films simultaneously. As the sidewall of the electroformed metal, the surface morphology and dimensional precision of the adhesive film are crucial to the subsequent electroforming process. Through dimensional check of the fabricated film prototype, the manufacturing tolerance is kept within an acceptable range.

B. Electroforming

The photoresist SU-8 2015 mold is then used to fabricate the metallic TA layers. A mirror stainless steel is chosen as the electroforming substrate, so it is unnecessary to take the conductive pretreatment and sacrificial layer preparation into consideration. The uniformity of the bottom surface of the electroformed layer can be guaranteed due to its extremely low surface roughness, which prevents UV dispersion on the metal surface during exposure. Two electrodes, an anode and a cathode, are involved in the electroforming process, which is based on electrochemical reactions. After a serious of pre-experiments, the composition of the electroforming electrolyte is determined, listed in Table IV.

In accordance with the Butler-Volmer equation, the activation overpotential rises as the electrode current density increases, resulting in the refining of grain [53]. As illustrated in Fig. 8, four distinct electroformed copper surfaces are exhibited at varying dc current densities while the solution is agitated with a magnetic stirrer. Low density of current leads to missed electroforming; Increasing current density refines the grains, whereas excessive current density coarsens the grains and produces stripes. Hence, the current density must be carefully adjusted. The thickness of the electroformed layer δ is directly proportional to the current density I and electroforming time t, which can be expressed as

$$\delta = \frac{100KIt\eta}{S\rho}. \tag{3}$$

The quantities K, η, S, and ρ represent the electrochemical equivalent, current efficiency, electroforming area, and metal density, respectively. In reality, the current is not uniformly distributed across the substrate, but is more concentrated at the margins, resulting in defects in the casting layer that are thin in the center and thick at the edges. In this case, the assembly area can serve as an on-chip auxiliary cathode. The electric field lines are concentrated at the assembly area's perimeter, whereas their current density is relatively average in the interior core region.

Authorized licensed use limited to: CHINA UNIVERSITY OF MINING AND TECHNOLOGY. Downloaded on March 07,2024 at 00:09:57 UTC from IEEE Xplore. Restrictions apply.

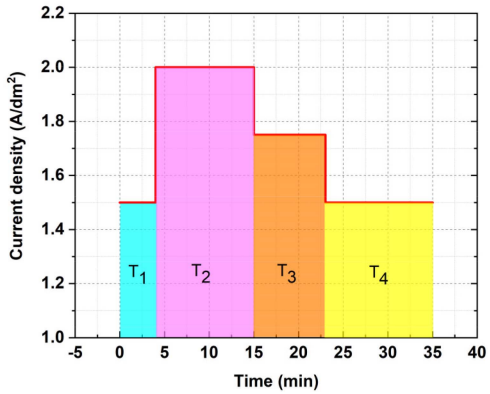

Fig. 9. Arrangement of the segmented electroforming time. (1) T_1: Charge the electrode plate at a lower current density, and coat the surface of the activated substrate with a thin layer of copper. (2) T_2: Increase the current density and refine the grain. (3) T_3: Reduce the current density, reduce the asymmetrical thickness distribution brought on by concentration polarization, and fill the majority of the die's internal areas with forward pulse current. (4) T_4: Adopt the optimal current density under dc for metal surface refinement.

In the actual electroforming process, it can be discovered that when filling the copper metal in the concave mold with a lower current density using conventional dc electroforming, it is often challenging to fill completely, leading to pits or even cavities. Increasing the current density cannot remedy the problem at this time, and there are evidently filling defects with a narrow middle and broad four sides. During electroforming, the mass transfer capacity of the solution can be enhanced with a magnetic stirrer, and a low current density is employed at the beginning of the process to assure the required bonding strength. As shown in Fig. 9, stepped electroforming is performed with various current densities.

At the end of the electroforming process, two additional processes are necessary to obtain the desired single metal-only layer with folded slots. The first step is to remove the SU-8 structures. Considering the characteristic of longitudinal penetration of each single-layer structure, such a removal operation is not difficult. Marginally cross-linked SU-8 structures will swell and detach when exposed to the solvent Remover PG provided by MiroChem. The deionized water must be utilized to remove any remaining adhesive. Second, separating the copper layer structure from the wafer constitutes the next stage. Due to the smooth surface of mirror stainless steel, the bonding force between the wafer and copper layer is relatively weak. Fig. 10 shows a photography of the fabricated single metal-only folded-slot layer stripped from the wafer. To observe more details of the fabricated sample, an SEM view is also presented in Fig. 11. Through multiple measurements of the sample by an optical profilometer (KEYENCE VHX-6000), the average surface roughness R_a can be controlled within 0.2 μm. Therefore, the sample has no photoresist residue, fractures, or burrs, and its side wall is perpendicular and smooth. In addition, all the shim layers can be fabricated with the same process as these folded-slot layers but without the periodic structure in the central area. The thickness of the shim layer will increase to 60 μm with the extension of electroforming time.

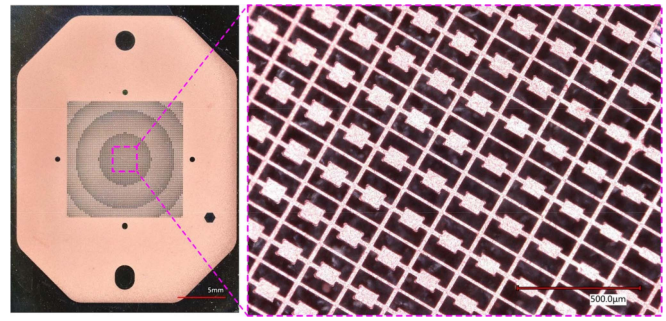

Fig. 10. Photography of the fabricated single metal-only folded-slot layer after the electroforming.

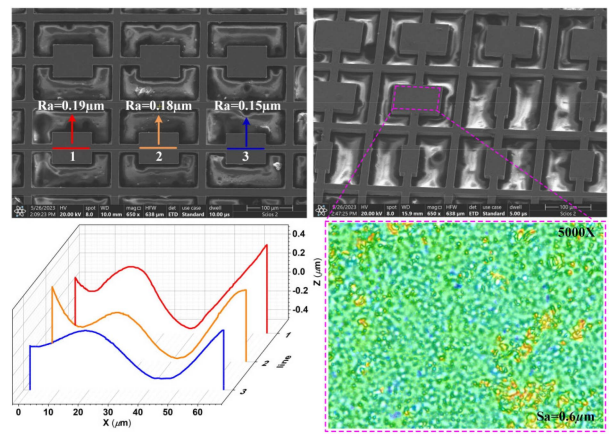

Fig. 11. SEM images of the fabricated metal-only folded-slot layer and the measurement of its surface roughness.

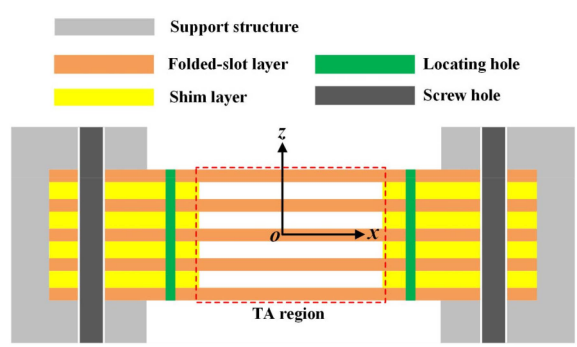

Fig. 12. Assembly diagram of all the metallic layers.

C. Assembly

The final step involves the precise assembly of all metallic layers, which include five folded-slot layers and four air-filled spacer layers. As shown in Fig. 12, these copper layers are stacked in sequence. These pinholes, the accuracy of whose placement can be guaranteed by the photolithography process, can be used to position all the copper layers. During the fabrication and assemblage of the copper layers, it is impossible to completely eliminate internal stresses, which may impact the precision of the assembly. To prevent the copper layers from deforming, a series of 3-D-printed support structures have been

Authorized licensed use limited to: CHINA UNIVERSITY OF MINING AND TECHNOLOGY. Downloaded on March 07,2024 at 00:09:57 UTC from IEEE Xplore. Restrictions apply.

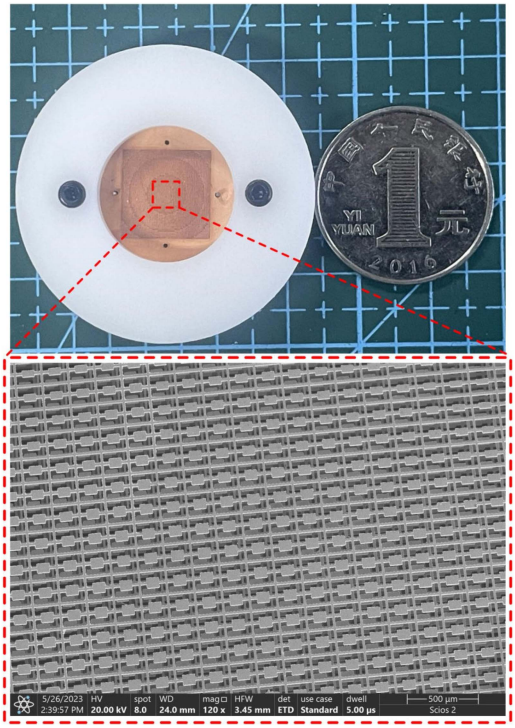

Fig. 13. Photography of the assembled metal-only TA with its SEM view.

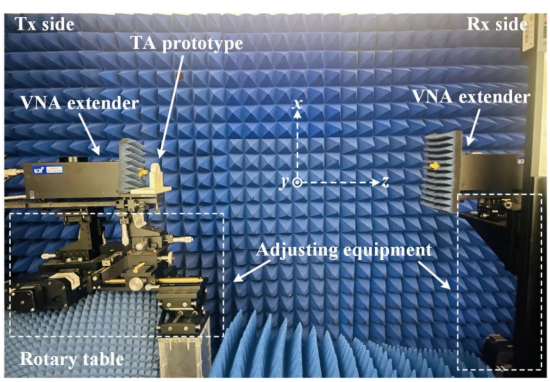

Fig. 14. Measurement setup for the THz metal-only TA antenna.

fabricated. Each copper layer is marked with a hexagonal alignment indicator. Finally, Fig. 13 shows the assembled metal-only TA prototype with its SEM view.

IV. Measurement and Discussion

A. Experiment of the THz TA Antenna

As shown in Fig. 14, the microfabricated THz metal-only TA antenna can be experimentally verified in a THz anechoic chamber. The reflection coefficients and radiation performances are measured utilizing a vector network analyzer with two VDI frequency extension modules. For precise adjustment of the relative position between the feed source and the micromachined TA prototype, a set of high-precision manually-moving stages are employed in this experiment. On the electronic rotary table, the TA prototype should be located at the rotational center. It should be noted that the IF bandwidth is set to 1 Hz to provide a maximal signal-to-noise ratio in the experiment. To satisfy the far-field condition, the receiver and transmitter must be separated by more than 0.8 m. The input power to the TA antenna is set to 2 mW in the measurement.

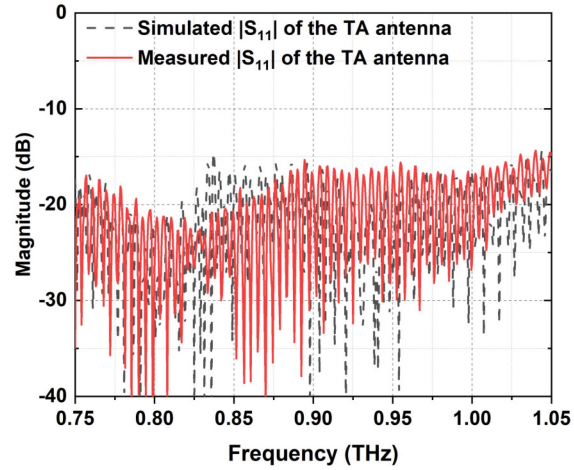

Fig. 15. Reflection coefficients of the THz metal-only TA antenna.

TABLE V
Details of the Radiation Patterns of the TA Antenna

Frequency		0.8 THz		0.9 THz		1.0 THz	
Plane		E	H	E	H	E	H
CPL (dB)	Sim.	< -70	< -70	< -75	< -70	< -65	< -70
	Mea.	-25.7	-26.8	-26.6	-26.9	-23.7	-26.4
SLL (dB)	Sim.	-19.9	-21.2	-23.9	-24.5	-18.0	-19.1
	Mea.	-17.8	-20.4	-23.5	-23.7	-19.1	-18.4
HPBW (°)	Sim.	2.0	2.0	1.7	1.7	1.7	1.7
	Mea.	2.1	2.0	1.8	1.8	1.7	1.8
FNBW (°)	Sim.	8.3	8.4	6.3	6.4	8.7	9.1
	Mea.	9.0	8.2	6.8	6.8	5.8	7.6

The reflection coefficient of the whole TA antenna can be measured at the waveguide port of the diagonal horn. Fig. 15 presents the measured $|S_{11}|$ results of the whole TA antenna from 0.75 to 1.05 THz, as well as the simulated results for comparison; both are below -15 dB. To obtain accurate radiation patterns, the location of the diagonal horn and the metal-only TA must be precisely adjusted. The radiation patterns at *E*-plane and *H*-plane cuts can be scanned by rotating the TA antenna. Fig. 16 illustrates the normalized radiation patterns at three THz frequency points. Table V provides essential information regarding the simulated and measured radiation patterns, including the CPL, the side-lobe level (SLL), the HPBW, and the first-null beamwidth (FNBW). The measured radiation patterns in Fig. 16 correspond well with the simulations close to the directions within the main lobe. Due to the constrained dynamic range of the THz VNA and the weak THz signal received, measurement errors lead to a large discrepancy in nonmain-lobe areas. The gain and the efficiency of the metal-only TA antenna are plotted in Fig. 17. The measured result of the peak gain within the operation band is 36.47 dBi at 0.91 THz, and its corresponding aperture efficiency is about 25.96%. The measured 3-dB gain bandwidth is between 0.79 and 1.03 THz, about 26.67% with respect to 0.9 THz. It

Authorized licensed use limited to: CHINA UNIVERSITY OF MINING AND TECHNOLOGY. Downloaded on March 07,2024 at 00:09:57 UTC from IEEE Xplore. Restrictions apply.

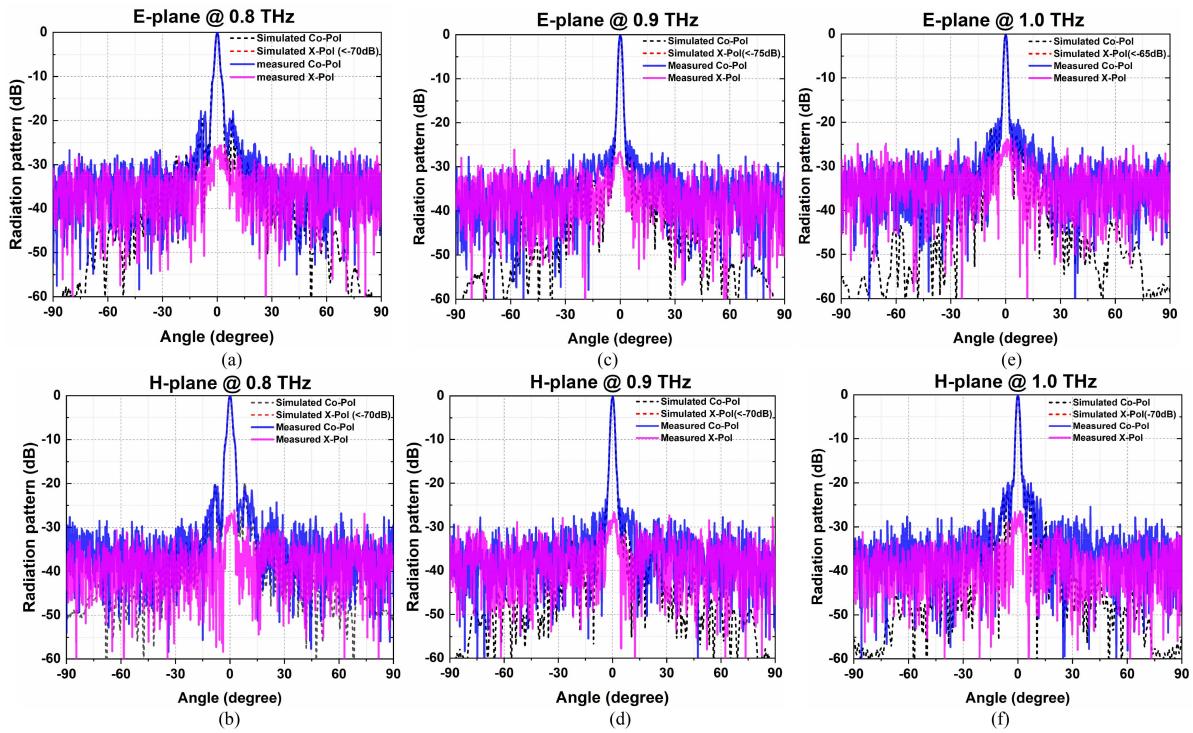

Fig. 16. Radiation patterns of the THz metal-only TA antenna. (a) E-plane at 0.8 THz. (b) H-plane at 0.8 THz. (c) E-plane at 0.9 THz. (d) H-plane at 0.9 THz. (e) E-plane at 1.0 THz. (f) H-plane at 1.0 THz.

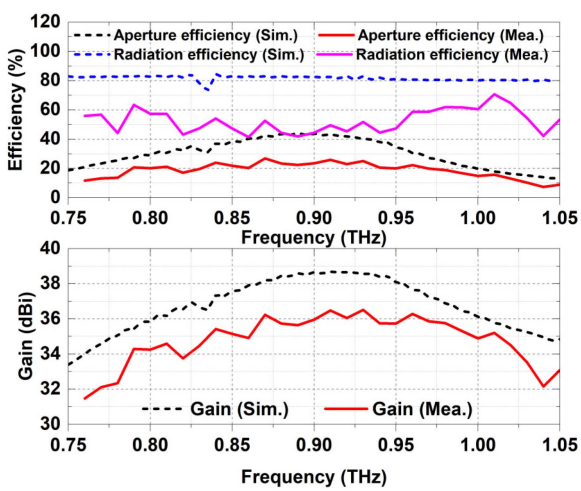

Fig. 17. Simulated and measured gain and corresponding efficiency within the frequency band of interest.

differs from the bandwidth of the MFSS TA element because the antenna gain bandwidth can be affected by many factors, including the array construction approach, fabrication errors, and misalignment in the experiment.

B. Error Analysis

The fact that the average gain difference between simulated and measured results for the operating band is greater than 2.5 dB cannot be ignored. As shown in Fig. 18, there have been full-wave simulations conducted to investigate some potential causes for the gain difference, such as the surface roughness, the feed source excursion in the measurement, the misalignment of the metallic layers, and the air spacer thickness deviation. First, the roughness of the metal-only TA surfaces can be analyzed using the Hall-Huray theory, a well-recognized method for modeling uneven surfaces [54], [55]. The two metrics, namely nodule radius (NR) and surface ratio (SR), can be used to characterize each exterior surface of the metal-only TA, which resembles an irregular assortment of nodules. Some simulations for the metal-only unit cell are performed to evaluate the surface roughness influence. Under different settings of {NR, SR}, the simulated magnitudes of the elements at 0.9 THz, shown in Fig. 18(a), are presented when the parameter l_1 changes from 15 to 107 μm by the step of 2 μm. Observably, the transmission magnitude decreases as the two parameters increase, which can lead to a decrease in the measured gain. Second, feed source excursion is one of the typical TA measurement errors. In order to study this effect, the THz diagonal horn is shifted 150 μm in various directions. As shown in Fig. 18(b), the gain of the TA antenna decreases if the phase center of the source deviates from the focal point, especially along the x- and y-direction shown in Fig. 14. Third, given that all of the metallic folded-slot layers and shim layers must be stacked accurately in order, it seems inevitable that an assembly error will occur. As shown in Fig. 18(c), three misalignment cases are analyzed assuming that there is no offset for the first folded-slot layer. It can be observed that the simulated gain drops when additional misalignment, such as dislocation of these metallic layers, is incorporated into the antenna simulation. Fourth, some simulations with varying

Authorized licensed use limited to: CHINA UNIVERSITY OF MINING AND TECHNOLOGY. Downloaded on March 07,2024 at 00:09:57 UTC from IEEE Xplore. Restrictions apply.

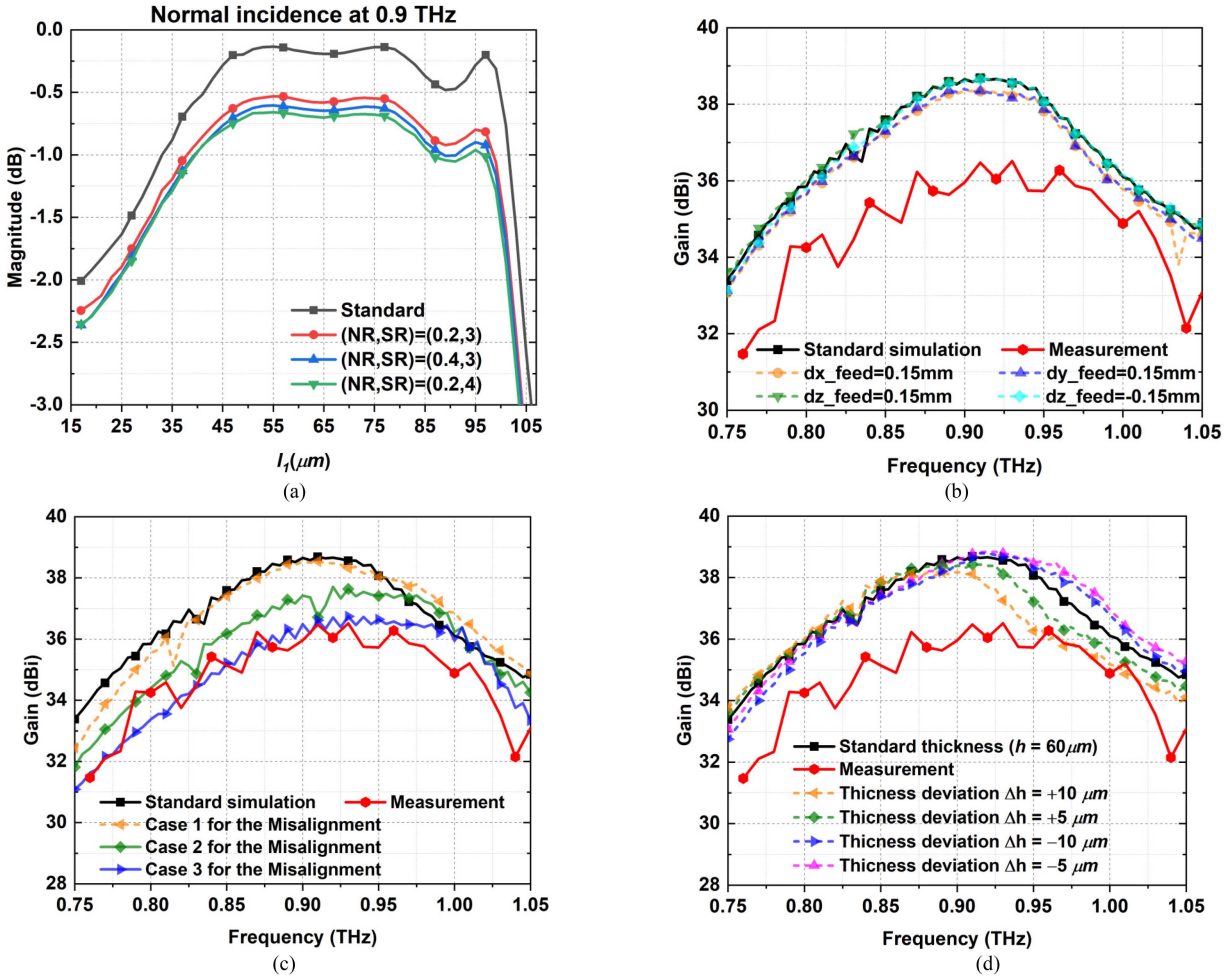

Fig. 18. Error analysis on some potential effects. (a) Surface roughness. (b) Feed source excursion. (c) Misalignment. Case 1 for the misalignment: $\{dx_2, dy_2; dx_3, dy_3; dx_4, dy_4; dx_5, dy_5\} = \{20, 20; -20, -20; 20, 20; -20, -20\}\mu$m; Case 2 for the misalignment: $\{dx_2, dy_2; dx_3, dy_3; dx_4, dy_4; dx_5, dy_5\} = \{30, 30; -30, 30; -30, -30; 30, -30\}\mu$m; Case 3 for the misalignment: $\{dx_2, dy_2; dx_3, dy_3; dx_4, dy_4; dx_5, dy_5\} = \{40, 40; -40, 40; -40, -40; 40, -40\}\mu$m. The parameters dx and dy represent the x- and y-direction offsets, respectively. The subscript represents the layer number, and the first layer is the one closest to the feed source. (d) Air spacer thickness deviation.

thickness deviations are also performed to investigate the sensitivity of air spacer thickness deviation. As shown in Fig. 18(d), the simulated gain is significantly impacted by variations in the thickness of the shim layers, particularly in close proximity to the high operating frequency range. However, all the shim layers can be manufactured using the same process as these folded-slot metallic layers. The electroforming time permits micrometer-level precision in controlling the thickness of these air spacers. It is improbable that such a thickness of offset would occur for the prototype. In summary, such a gain discrepancy is caused by the aforementioned combined effects.

C. Discussion

In Table VI, the proposed 1.0-THz metal-only TA antenna micromachined by UV-LIGA technology is compared to various kinds of state-of-the-art THz antennas with high-gain performance, including horns, planar arrays, reflectors, lenses, reflectarrays, and TAs. All of these THz antennas have been well implemented utilizing suitable processes. As a planar version of lens antennas, TAs have been identified as one of the good candidates for high-gain THz applications. Some conventional processes, such as 3-D printing, PCB, and LTCC, can still be used to manufacture TAs in the low THz regions. However, when the operating frequency reaches the high THz frequency regions, e.g., at or above the WR-1.0 band, geometrical accuracy and machining tolerance pose significant challenges for the implementation of THz TAs. Noting that high-gain metal-only TAs correspond to an electrically large radiation aperture, the thickness of each metallic layer should not be too thin for structural stability. In light of the need for layers with a high aspect ratio, high precision, low surface imperfection, and a high yield, the UV-LIGA technology offers a versatile and efficient method for fabricating THz metal-only TAs up to the WR-1.0 band.

Some obvious differences can be observed between the simulated and measured results. We investigate some potential causes for these discrepancies. On the one hand, measurement errors cause a large discrepancy due to the limited dynamic range of the WR-1.0 VNA and the weak THz signal received. The

Authorized licensed use limited to: CHINA UNIVERSITY OF MINING AND TECHNOLOGY. Downloaded on March 07,2024 at 00:09:57 UTC from IEEE Xplore. Restrictions apply.

TABLE VI
COMPARISON WITH SOME EXISTING WORKS ON THz HIGH-GAIN ANTENNAS

Reference	Type	Process	Center frequency f_0 (THz)	Aperture size (mm^2)	Gain at f_0 (dBi/dBic)	3-dB Gain bandwidth (%)	CPL (dB)	SLL (dB)
[7]	Metallic horn	Milling	1.9	5	31.7	21.05	-20	–
[9]	Dielectric horn	DRIE	0.875	1.8	12	28.6	-10	–
[10]	Planar slot array	DRIE	0.36	810	38	22.22	–	-12
[12]	Planar patch array	SiGe	0.34	1.21	7.9	5	–	–
[14]	Planar array and PRS	DRIE	1.04	7.07	20.3	4.81	–	-16
[16]	Reflector	SiC sintering	0.33	215448	55.3	–	–	-32
[17]	Reflector	CNC	0.4	88	28.5	37.5	-32	-9
[21]	Folded RA	Lithography & PCB	0.39	309.15	32.84	16	-28.4	-17.8
[22]	Folded RA	DRIE	1	81	33.4	7	–	-15.9
[24]	Dielectric lens	CNC	0.29	314.16	29	30	–	12
[26]	Metallic lens	CNC	0.4125	600	27.6	14.5	-30	-10
[27]	Dielectric TA	3-D Printing	0.3	284.12	27.4	15.1	-20	-22
[29]	TA	PCB	0.28	400	32.2	25.1	–	-15
[30]	TA	PCB	0.145	1814.76	33	17.9	-23.5	-16
[31]	TA	LTCC	0.14	1600	33.12	24.4	-31	-21
[32]	TA	LTCC	0.27	669.67	20.8	3.4	-45	-13
[49]	Metal-only TA	Lithography and electroplating	0.34	2733.97	34.9	11.76	–	-22.1
This work	**Metal-only TA**	**UV-LIGA**	**0.9**	**147.87**	**35.96**	**26.67**	**-26.6**	**-23.5**

radiation performance, including the CPLs, SLLs, and FNBWs, can be significantly affected by the noise when the received signal is weak. On the other hand, fabrication and assembly defects have a significant impact on the TA antenna's measured performance. As previously discussed, these discrepancies can be caused by the combination of a number of factors, including surface roughness, input source deviation during measurement, misalignment of metallic layers, and air spacer thickness variation. Therefore, research must be conducted meticulously to enhance our fabrication and measurement technologies.

Finally, the present M-FSS metallic TA element has certain drawbacks, most notably the comparatively greater number of metallic layers, which may lead to an increase in fabrication complexity and a high profile. Two additional techniques can be used to reduce the number of metallic layers in TA antennas, as demonstrated at microwave and mm-wave frequencies [47], [56]. One consists of metal-only slot TA elements with polarization-rotation capability [47]. This unit cell design utilizes only three metallic layers and relies on the rotation technique, but the additional polarization-rotation property is rarely required in practice. The other one is the metal-only TA element based on Huygens' resonances [56]. This form of unit cells employs just two metallic layers to achieve a 360° phase shift with a high transmission amplitude. Nonetheless, compared to the proposed MFSS TA element, the Huygens' unit cells have a frequency band that is always more restricted.

V. CONCLUSION

The UV-LIGA technology enables the fabrication of high-precision THz metal-only TAs with miniature geometric features on a small scale of several micrometers. A 1.0-THz high-gain metal-only TA antenna is designed, fabricated, and measured in this article. A five-layered folded-slot element with four air gaps is presented for 360° phase coverage and high transmission amplitude. All of the metallic layers can be produced by the UV-LIGA technology simultaneously with two core steps, film fabrication and copper electroforming. After accurate assembly, the proposed metal-only TA is verified in a THz chamber. The peak value of the measured gain is 36.47 dBi at 0.91 THz, with an aperture efficiency of 25.96%. A 3-dB gain bandwidth of 0.79–1.03 THz (26.67%) can be achieved by the proposed TA antenna according to the measurement.

VI. AUTHOR CONTRIBUTIONS

Z.-W. Miao designed and measured the antenna. Z.-C. Hao and W. Hong proposed the idea and the system solution. Y. Zeng and D. Zhu proposed the high-precision fabrication process. Z. Liu fabricated the antenna. J.-H. Zhao and C.-Y. Ding contributed to the test for the extremely high-frequency antenna. L. Chen and L. Zhao contributed the antenna design and analysis.

REFERENCES

[1] H. J. Song and T. Nagatsuma, "Present and future of terahertz communications," *IEEE Trans. THz Sci. Technol.*, vol. 1, no. 1, pp. 256–263, Sep. 2011, doi: 10.1109/TTHZ.2011.2159552.

[2] I. F. Akyildiz, C. Han, Z. Hu, S. Nie, and J. M. Jornet, "Terahertz band communication: An old problem revisited and research directions for the next decade," *IEEE Trans. Commun.*, vol. 70, no. 6, pp. 4250–4285, Jun. 2022, doi: 10.1109/TCOMM.2022.3171800.

[3] Z. Chen et al., "A survey on terahertz communications," *China Commun*, vol. 16, no. 2, pp. 1–35, Feb. 2019, doi: 10.12676/j.cc.2019.02.001.

[4] Y. He, Y. Chen, L. Zhang, S. Wong, and Z. Chen, "An overview of terahertz antennas," *China Commun*, vol. 17, no. 7, pp. 124–165, Jul. 2020, doi: 10.23919/J.CC.2020.07.011.

Authorized licensed use limited to: CHINA UNIVERSITY OF MINING AND TECHNOLOGY. Downloaded on March 07,2024 at 00:09:57 UTC from IEEE Xplore. Restrictions apply.

[5] K. R. Jha and G. Singh, "Terahertz planar antennas for future wireless communication: A technical review," *Infr. Phys. Technol.*, vol. 60, pp. 71–80, Sep. 2013, doi: 10.1016/j.infrared.2013.03.009.

[6] S. Bhardwaj and J. L. Volakis, "Hexagonal waveguide based circularly polarized horn antennas for sub-mm-wave/terahertz band," *IEEE Trans. Antennas Propag.*, vol. 66, no. 7, pp. 3366–3374, Jul. 2018, doi: 10.1109/TAP.2018.2829842.

[7] N. Chahat et al., "1.9-THz Multiflare angle horn optimization for space instruments," *IEEE Trans. THz Sci. Technol.*, vol. 5, no. 6, pp. 914–921, Nov. 2015, doi: 10.1109/TTHZ.2015.2487781.

[8] A. Gonzalez, K. Kaneko, T. Kojima, S. Asayama, and Y. Uzawa, "Terahertz corrugated horns (1.25–1.57 THz): Design, Gaussian modeling, and measurements," *IEEE Trans. THz Sci. Technol.*, vol. 7, no. 1, pp. 42–52, Jan. 2017, doi: 10.1109/TTHZ.2016.2634860.

[9] H. Zhu, Q. Xue, J. Hui, and S. Pang, "A 750–1000 GHz H-plane dielectric horn based on silicon technology," *IEEE Trans. Antennas Propag.*, vol. 64, no. 12, pp. 5074–5083, Dec. 2016, doi: 10.1109/TAP.2016.2620471.

[10] A. Gomez-Torrent et al., "A 38 dB gain, low-loss, flat array antenna for 320–400 GHz enabled by silicon-on-insulator micromachining," *IEEE Trans. Antennas Propag.*, vol. 68, no. 6, pp. 4450–4458, Jun. 2020, doi: 10.1109/TAP.2020.2969753.

[11] K. Sarabandi, A. Jam, M. Vahidpour, and J. East, "A novel frequency beam-steering antenna array for submillimeter-wave applications," *IEEE Trans. THz Sci. Technol.*, vol. 8, no. 6, pp. 654–665, Nov. 2018, doi: 10.1109/TTHZ.2018.2866019.

[12] X. Deng, Y. Li, W. Wu, and Y. Xiong, "340-GHz SIW cavity-backed magnetic rectangular slot loop antennas and arrays in silicon technology," *IEEE Trans. Antennas Propag.*, vol. 63, no. 12, pp. 5272–5279, Dec. 2015, doi: 10.1109/TAP.2015.2490248.

[13] K. Luk et al., "A microfabricated low-profile wideband antenna array for terahertz communications," *Sci. Rep.*, vol. 7, 2017, Art. no. 1268, doi: 10.1038/s41598-017-01276-4.

[14] S. Zhu, Y. Li, K. Luk, and S. Pang, "Compact high-gain Si-imprinted THz antenna for ultrahigh speed wireless communications," *IEEE Trans. Antennas Propag.*, vol. 68, no. 8, pp. 5945–5954, Aug. 2020, doi: 10.1109/TAP.2020.2986863.

[15] A. Abohmra et al., "An ultrawideband microfabricated gold-based antenna array for terahertz communication," *IEEE Antennas Wireless Propag. Lett.*, vol. 20, no. 11, pp. 2156–2160, Nov. 2021, doi: 10.1109/LAWP.2021.3072562.

[16] H. Wang et al., "Terahertz high-gain offset reflector antennas using SiC and CFRP material," *IEEE Trans. Antennas Propag.*, vol. 65, no. 9, pp. 4443–4451, Sep. 2017, doi: 10.1109/TAP.2017.2724582.

[17] K. Fan, Z. Hao, Q. Yuan, and W. Hong, "Development of a high gain 325–500 GHz antenna using quasi-planar reflectors," *IEEE Trans. Antennas Propag.*, vol. 65, no. 7, pp. 3384–3391, Jul. 2017, doi: 10.1109/TAP.2017.2705022.

[18] C. Wang et al., "0.34-THz wireless link based on high-order modulation for future wireless local area network applications," *IEEE Trans. THz Sci. Technol.*, vol. 4, no. 1, pp. 75–85, Jan. 2014, doi: 10.1109/TTHZ.2013.2293119.

[19] H. Hasani et al., "Tri-band, polarization-independent reflectarray at terahertz frequencies: Design, fabrication, and measurement," *IEEE Trans. THz Sci. Technol.*, vol. 6, no. 2, pp. 268–277, Mar. 2016, doi: 10.1109/TTHZ.2016.2522301.

[20] S. Qu et al., "Frequency-controlled 2-D focus-scanning terahertz reflectarrays," *IEEE Trans. Antennas Propag.*, vol. 67, no. 3, pp. 1573–1581, Mar. 2019, doi: 10.1109/TAP.2018.2888949.

[21] Z. Miao et al., "A 400-GHz high-gain quartz-based single layered folded reflectarray antenna for terahertz applications," *IEEE Trans. THz Sci. Technol.*, vol. 9, no. 1, pp. 78–88, Jan. 2019, doi: 10.1109/TTHZ.2018.2883215.

[22] S. Zhu, G. Wu, S. Pang, and C. Chan, "Compact terahertz dielectric folded metasurface," *Adv. Opt. Mater.*, vol. 10, 2022, Art. no. 2101663, doi: 10.1002/adom.202101663.

[23] N. Llombart et al., "Silicon micromachined lens antenna for THz integrated heterodyne arrays," *IEEE Trans. THz Sci. Technol.*, vol. 3, no. 5, pp. 515–523, Sep. 2013, doi: 10.1109/TTHZ.2013.2270300.

[24] K. Konstantinidis et al., "Low-THz dielectric lens antenna with integrated waveguide feed," *IEEE Trans. THz Sci. Technol.*, vol. 7, no. 5, pp. 572–581, Sep. 2017, doi: 10.1109/TTHZ.2017.2725487.

[25] R. Zatta, V. S. Jagtap, J. Grzyb, and U. R. Pfeiffer, "Broadband lens-integrated CMOS camera-type THz compact antenna test range," *IEEE Trans. THz Sci. Technol.*, vol. 11, no. 5, pp. 527–537, Sep. 2021, doi: 10.1109/TTHZ.2021.3088286.

[26] Z. Hao, J. Wang, Q. Yuan, and W. Hong, "Development of a low-cost THz metallic lens antenna," *IEEE Antennas Wireless Propag. Lett.*, vol. 16, pp. 1751–1754, 2017, doi: 10.1109/LAWP.2017.2671880.

[27] G. Wu, Y. Zeng, K. Chan, S. Qu, and C. Chan, "3-D printed circularly polarized modified fresnel lens operating at terahertz frequencies," *IEEE Trans. Antennas Propag.*, vol. 67, no. 7, pp. 4429–4437, Jul. 2019, doi: 10.1109/TAP.2019.2908110.

[28] J. Zhu, Y. Yang, D. McGloin, S. Liao, and Q. Xue, "Sub-terahertz 3-D printed all-dielectric low-cost low-profile lens-integrated polarization beam splitter," *IEEE Trans. THz Sci. Technol.*, vol. 11, no. 4, pp. 433–442, Jul. 2021, doi: 10.1109/TTHZ.2021.3064209.

[29] O. Koutsos, F. Manzillo, A. Clemente, and R. Sauleau, "Analysis, rigorous design, and characterization of a three-layer anisotropic transmitarray at 300 GHz," *IEEE Trans. Antennas Propag.*, vol. 70, no. 7, pp. 5437–5446, Jul. 2022, doi: 10.1109/TAP.2022.3145506.

[30] F. Manzillo, A. Clemente, and J. González-Jiménez, "High gain D-band transmitarrays in standard PCB technology for beyond 5G communications," *IEEE Trans. Antennas Propag.*, vol. 68, no. 1, pp. 587–592, Jan. 2020, doi: 10.1109/TAP.2019.2938630.

[31] Z. Miao et al., "140 GHz high-gain LTCC-integrated transmit-array antenna using a wideband SIW aperture-coupling phase delay structure," *IEEE Trans. Antennas Propag.*, vol. 66, no. 1, pp. 182–190, Jan. 2018, doi: 10.1109/TAP.2017.2776345.

[32] J. Xu, Z. Chen, and X. Qing, "270-GHz LTCC-integrated high gain cavity-backed Fresnel zone plate lens antenna," *IEEE Trans. Antennas Propag.*, vol. 61, no. 4, pp. 1679–1687, Apr. 2013, doi: 10.1109/TAP.2012.2232261.

[33] J. Huang and J. A. Encinar, *Reflectarray Antennas*. Hoboken, NJ, USA: Wiley, 2008.

[34] S. Koenig et al., "Wireless sub-THz communication system with high data rate," *Nature Photon*, vol. 7, pp. 977–981, Dec. 2013, doi: 10.1038/nphoton.2013.275.

[35] G. Ducournau et al., "Ultrawide-bandwidth single-channel 0.4-THz wireless link combining broadband quasi-optic photomixer and coherent detection," *IEEE Trans. THz Sci. Technol.*, vol. 4, no. 3, pp. 328–337, May 2014, doi: 10.1109/TTHZ.2014.2309006.

[36] C. Ryan et al., "A wideband transmitarray using dual-resonant double square rings," *IEEE Trans. Antennas Propag.*, vol. 58, no. 5, pp. 1486–1493, May 2010, doi: 10.1109/TAP.2010.2044356.

[37] B. Rahmati and H. Hassani, "Low-profile slot transmitarray antenna," *IEEE Trans. Antennas Propag.*, vol. 63, no. 1, pp. 174–181, Jan. 2015, doi: 10.1109/TAP.2014.2368576.

[38] Q. Lou, C. Xue, and Z. N. Chen, "High-efficiency metalens antenna using Huygens' metasurface with glide symmetric I-shape metal strips," *IEEE Trans. Antennas Propag.*, vol. 69, no. 11, pp. 7394–7403, Nov. 2021, doi: 10.1109/TAP.2021.3083738.

[39] C. Jouanlanne et al., "Wideband linearly polarized transmitarray antenna for 60 GHz backhauling," *IEEE Trans. Antennas Propag.*, vol. 65, no. 3, pp. 1440–1445, Mar. 2017, doi: 10.1109/TAP.2017.2655018.

[40] G. Chattopadhyay, T. Reck, C. Lee, and C. Jung-Kubiak, "Micromachined packaging for terahertz systems," *Proc. IEEE*, vol. 105, no. 6, pp. 1139–1150, Jun. 2017, doi: 10.1109/JPROC.2016.2644985.

[41] N. Grady et al., "Terahertz metamaterials for linear polarization conversion and anomalous refraction," *Science*, vol. 340, no. 6138, pp. 1304–1307, May 2013, doi: 10.1126/science.1235399.

[42] S. Liu et al., "Anomalous refraction and nondiffractive Bessel-beam generation of terahertz waves through transmission-type coding metasurfaces," *ACS Photon*, vol. 3, no. 10, pp. 1968–1977, Sep. 2016, doi: 10.1021/acsphotonics.6b00515.

[43] A. Abdelrahman, A. Elsherbeni, and F. Yang, "Transmission phase limit of multilayer frequency-selective surfaces for transmitarray designs," *IEEE Trans. Antennas Propag.*, vol. 62, no. 2, pp. 690–697, Feb. 2014, doi: 10.1109/TAP.2013.2289313.

[44] A. Abdelrahman, A. Elsherbeni, and F. Yang, "Transmitarray antenna design using cross-slot elements with no dielectric substrate," *IEEE Antennas Wireless Propag. Lett.*, vol. 13, pp. 177–180, 2014, doi: 10.1109/LAWP.2014.2298851.

[45] R. Wu, Y. Li, W. Wu, C. Shi, and T. Cui, "High-gain dual-band transmitarray," *IEEE Trans. Antennas Propag.*, vol. 65, no. 7, pp. 3481–3488, Jul. 2017, doi: 10.1109/TAP.2017.2705074.

[46] J. Zhao et al., "A novel planar mode-transducing antenna based on metal-only transmitarray surfaces," *IEEE Trans. Antennas Propag.*, vol. 67, no. 6, pp. 3762–3773, Jun. 2019, doi: 10.1109/TAP.2019.2902709.

[47] K. Pham et al., "Low-cost metal-only transmitarray antennas at Ka-band," *IEEE Antennas Wireless Propag. Lett.*, vol. 18, no. 6, pp. 1243–1247, Jun. 2019, doi: 10.1109/LAWP.2019.2913571.

Authorized licensed use limited to: CHINA UNIVERSITY OF MINING AND TECHNOLOGY. Downloaded on March 07,2024 at 00:09:57 UTC from IEEE Xplore. Restrictions apply.

[48] W. Hu et al., "A wideband metal-only transmitarray with two-layer configuration," *IEEE Antennas Wireless Propag. Lett.*, vol. 20, no. 7, pp. 1347–1351, Jul. 2021, doi: 10.1109/LAWP.2021.3081445.
[49] G. Liu, H. Wang, J. Jiang, and F. Xue, "Terahertz substrateless transmitarray antenna design and microfabrication," *Microw. Opt. Technol. Lett.*, vol. 58, no. 9, pp. 2096–2100, Sep. 2016, doi: 10.1002/mop.29985.
[50] W. Bacher, W. Menz, and J. Mohr, "The LIGA technique and its potential for microsystems-a survey," *IEEE Trans. Ind. Electron.*, vol. 42, no. 5, pp. 431–441, Oct. 1995, doi: 10.1109/41.464604.
[51] A. Malekabadi and C. Paoloni, "UV-LIGA microfabrication process for sub-terahertz waveguides utilizing multiple layered SU-8 photoresist," *J. Micromech. Microeng.*, vol. 26, no. 9, 2016, Art. no. 095010, doi: 10.1088/0960-1317/26/9/095010.
[52] Available on the website [Online]. Available: https://vadiodes.com/en/products/straight-waveguides-tapers-horn-antenna-directional-couplers
[53] E. Dickinson and A. Wain, "The Butler-Volmer equation in electrochemical theory: Origins, value, and practical application," *J. Electroanal. Chem.*, vol. 872, Sep. 2020, Art. no. 114145, doi: 10.1016/j.jelechem.2020.114145.
[54] P. Huray et al., "Fundamentals of a 3-D 'snowball' model for surface roughness power losses," in *Proc. IEEE Workshop Signal Propag. Interconnects*, 2007, pp. 121–124, doi: 10.1109/SPI.2007.4512227.
[55] S. Hall et al., "Multigigahertz causal transmission line modeling methodology using a 3-D hemispherical surface roughness approach," *IEEE Trans. Microw. Theory Techn.*, vol. 55, no. 12, pp. 2614–2624, Dec. 2007, doi: 10.1109/TMTT.2007.910076.
[56] D. Su et al., "A double-layer metal-only Huygens' metasurface transmitarray," *IEEE Antennas Wireless Propag. Lett.*, vol. 22, no. 8, pp. 1897–1901, Aug. 2023, doi: 10.1109/LAWP.2023.3269075.

Zhuo-Wei Miao (Member, IEEE) received the B.S. degree in electronics and information engineering from Nanjing Normal University, Nanjing, China, in 2014, and the Ph.D. degree in electromagnetic field and microwave technology from Southeast University, Nanjing, in 2020.

From 2019 to 2020, he was a Visiting Ph.D. student with the Department of Electrical and Computer Engineering, National University of Singapore, Singapore. He is currently a Research Fellow with the State Key Laboratory of Millimeter Waves, School of Information Science and Engineering, Southeast University. His current research interests include millimeter-wave and terahertz antennas and circuits, terahertz systems, and metamaterials.

Zhenhao Liu was born in Weifang, China, in 2000. He received the B.S. degree in mechanical design, manufacturing, and automation from Wuhan University of Technology, Wuhan, China, in 2021. He is currently working toward the M.S. degree in mechanical engineering from the Nanjing University of Aeronautics and Astronautics, Nanjing, China.

His main research interests include nontraditional machining and micro fabrication.

Zhang-Cheng Hao (Senior Member, IEEE) received the B.S. degree in microwave engineering from Xidian University, Xi'an, China, in 1997, and the M.S. and Ph.D. degrees in radio engineering from Southeast University, Nanjing, China, in 2002 and 2006, respectively.

In 2006, he joined the Laboratory of Electronics and Systems for Telecommunications, École Nationale Supérieure des Télécommunications de Bretagne, Bretagne, France, as a Postdoctoral Researcher, where he was involved in developing millimeter-wave antennas. In 2007, he joined the Department of Electrical, Electronic and Computer Engineering, Heriot-Watt University, Edinburgh, U.K., as a Research Associate, where he was involved in developing multilayer integrated circuits and ultra-wide-band components. In 2011, he joined the School of Information Science and Engineering, Southeast University, as a Professor. He holds 20 granted patents and has authored or coauthored more than 200 referred journal and conference papers. His current research interests involve microwave and millimeter-wave systems, submillimeter-wave and terahertz components and passive circuits, including filters, antenna arrays, and multiple-beam technologies.

Dr. Hao is a member of the IEEE Microwave Theory and Technology Society's Technical Committee on Terahertz Technology and Applications (IEEE MTT-21). He has served as the TPC Chair or the Co-Chair for many international conferences, such as International Workshop on Antenna Technology (iWAT) 2018, International Conference on Microwave and Millimeter Wave Technology (ICMMT) 2019, International Symposium on Antennas and Propagation (ISAP) 2019, and so on. He has served as a Reviewer for many technique journals, including IEEE Transactions on Microwave Theory and Techniques (T-MTT), IEEE Transactions on Antennas and Propagation, IEEE Antennas and Wireless Propagation Letters, and IEEE Microwave and Wireless Components Letters, a Guest Editor for the Special Issue on International Wireless Symposium 2018 of the IEEE T-MTT, and an Associate Editor for the *IET Electronics Letters* and the *IET Microwaves Antennas, and Propagation*.

Yongbin Zeng received the B.S. and Ph.D. degrees in mechanical engineering from Nanjing University of Aeronautics and Astronautics, Nanjing, China, in 2002 and 2008, respectively.

After graduation, he joined the College of Mechanical & Electrical Engineering, Nanjing University of Aeronautics and Astronautics, Nanjing, China, as a Lecturer, and he was promoted to Associate Professor and Professor in 2011 and 2015, respectively. His current research interests include nontraditional machining, electrochemical micromachining, and micro/nanoscale fabrication.

Dr. Zeng has presided over more than 30 national and provincial projects such as the National Natural Science Foundation of China, Aviation Science Foundation, and Natural Science Foundation of Jiangsu Province. He has coauthored or authored more than 100 journal papers as the first author or coauthor and holds more than 40 granted patents. He has won the first Prize of National Defense Science and Technology and National Defense Innovation Group Award in 2010 and 2017, respectively.

Di Zhu received the M.S. and Ph.D. degrees in mechanical engineering from Nanjing University of Aeronautics and Astronautics, Nanjing, China, in 1981 and 1985, respectively.

From 1991 to 1992, he was a Research Fellow at the University of Liverpool, U.K. Since 1993, he has been a Professor with Nanjing University of Aeronautics and Astronautics. From 1995 to 1999, he was a Visiting Scholar with the University of Nebraska-Lincoln, Lincoln, NE, USA. His research interests include nontraditional machining, electrochemical micromachining, and micro/nanoscale fabrication.

Di Zhu is a Fellow of The International Academy for Production Engineering (CIRP). Since 2011, he has been a member of the China Academy of Sciences.

Authorized licensed use limited to: CHINA UNIVERSITY OF MINING AND TECHNOLOGY. Downloaded on March 07,2024 at 00:09:57 UTC from IEEE Xplore. Restrictions apply.

Jia-Hui Zhao (Student Member, IEEE) received the B.S. degree in electronic and information engineering from Northeastern University, Qinhuangdao, China, in 2021. She is currently working toward the Ph.D. degree in electromagnetic field and microwave technology at the State Key Laboratory of Millimeter Waves, Southeast University, Nanjing, China.

Her current research interests include tensor surfaces, high-gain antennas, low-profile transmitarray, and terahertz technology.

Chen-Yu Ding (Student Member, IEEE) received the B.S. degree in electromagnetic fields and wireless technology from Northwestern Polytechnical University, Xi'an, China, in 2020. He is currently working toward the Ph.D. degree in electromagnetic field and microwave technology at the State Key Laboratory of Millimeter Waves, Southeast University, Nanjing, China.

His current research interests include high-gain antenna array, multibeam antennas, and terahertz technology.

Li Cheng was born in Zhenjiang, China, in 1988. He received the B.S. degree in electronic engineering from University of Electronic Science and Technology of China, Chengdu, China, in 2011, and the Ph.D. degree in electromagnetic field and microwave technology from Southeast University, Nanjing, China, in 2017.

In 2018, he joined Nanjing Research Institute of Electronics Technology, Nanjing, China, where he is currently a Senior Engineer. His current research interests include millimeter-wave radar system and terahertz radar system design.

Lei Zhao (Senior Member, IEEE) received the B.S. degree in mathematics from Jiangsu Normal University, Xuzhou, China, in 1997, and the M.S. degree in computational mathematics and the Ph.D. degree in electromagnetic fields and microwave technology from Southeast University, Nanjing, China, in 2004 and 2007, respectively.

From 2007 to 2009, he worked with the Department of Electronic Engineering, The Chinese University of Hong Kong, Hong Kong, as a Research Associate. From 2009 to 2018, he worked with Jiangsu Normal University. During 2011, he worked with the Department of Electrical and Computer Engineering, National University of Singapore, Singapore, as a Research Fellow. From 2016 to 2017, he worked with the Department of Electrical and Computer Engineering, University of Illinois at Urbana-Champaign, Champaign, IL, USA, as a Visiting Scholar. He joined the China University of Mining and Technology, Xuzhou, China, in 2019, where he is currently a Full Professor. He has authored or coauthored more than 100 refereed journal and conference papers. His current research interests include spoof surface plasmon polaritons theory and its applications, RF/Microwave antenna and filter design, computational electromagnetics, and electromagnetic radiation to human's body.

Dr. Zhao serves as an Associate Editor for IEEE ACCESS, an Associate Editor-in-Chief for *ACES Journal*, and a Reviewer for multiple journals and conferences, including IEEE TRANSACTIONS ON MICROWAVE THEORY AND TECHNIQUES, IEEE TRANSACTIONS ON ANTENNAS AND PROPAGATION, IEEE ANTENNAS AND WIRELESS PROPAGATION LETTERS, *ACES Journal*, and other primary electromagnetics and microwave related journals.

Wei Hong (Fellow, IEEE) received the B.S. degree from the University of Information Engineering, Zhengzhou, China, in 1982, and the M.S. and Ph.D. degrees from Southeast University, Nanjing, China, in 1985 and 1988, respectively, all in radio engineering.

Since 1988, he has been with the State Key Laboratory of Millimeter Waves, Southeast University, where he is currently a Professor of the School of Information Science and Engineering. In 1993, 1995, 1996, 1997, and 1998, he was a short-term Visiting Scholar with the University of California at Berkeley, Berkeley, CA, USA, and the University of California at Santa Cruz, Santa Cruz, CA, USA. He has been engaged in numerical methods for electromagnetic problems, millimeter-wave theory and technology, antennas, and RF technology for wireless communications. He has authored and coauthored more than 300 technical publications and two books.

Dr. Hong is a Fellow of Chinese Institute of Electronics (CIE). He was an elected IEEE Microwave Theory and Technology Society (MTT-S) AdCom Member from 2014 to 2016. He has twice awarded the National Natural Prizes, four times awarded the first-class Science and Technology Progress Prizes issued by the Ministry of Education of China, and the Jiangsu Province Government, and the Foundations for China Distinguished Young Investigators and for "Innovation Group" issued by NSF of China. He is the Vice President of the CIE Microwave Society and Antenna Society and the Chair of the IEEE MTT-S/Antennas and Propagation Society (AP-S)/Electromagnetic Compatibility Society (EMC-S) Joint Nanjing Chapter. He has served as the Associate Editor for IEEE TRANSACTIONS ON MICROWAVE THEORY AND TECHNIQUES from 2007 to 2010.

Authorized licensed use limited to: CHINA UNIVERSITY OF MINING AND TECHNOLOGY. Downloaded on March 07,2024 at 00:09:57 UTC from IEEE Xplore. Restrictions apply.